Selective oxidation of ternary Fe-Mn-Si alloys during annealing process

Xue Zhang[a,b], Cauê Corrêa da Silva[a], Chang Liu[a], Manoj Prabhakar[a], Michael Rohwerder[a,*]

[a] Max-Planck-Institut für Eisenforschung GmbH, Max-Planck-Straße 1, Düsseldorf, 40237, Germany
[b] Laboratory for Corrosion and Protection, Institute of Metal Research, Chinese Academy of Sciences, Shenyang, 110016, China

ARTICLE INFO

ABSTRACT

Selective oxidation of Fe2MnxSi alloys with various Si contents annealed in a gas mixture of H_2/H_2O ($p(O_2)$ = 6.5×10^{-25} bar at 700 °C) for 2 h was investigated. The oxidation kinetics of all the alloys followed linear growth, indicating that most likely oxygen uptake was the rate-determining step. The addition of Si into Fe2Mn eliminated the formation of the ridge-like MnO at the surface, mainly on the grain boundaries, but significantly accelerated the internal oxidation especially along grain boundaries. The effects of Si on the external and internal oxidation including the morphology, distribution and chemistry of the oxides are discussed.

1. Introduction

High strength steels that normally contain small additions of manganese, silicon and/or aluminum (such as Dual Phase (DP) and Transformation Induced Plasticity (TRIP) steels) are widely used in the automotive industry due to their desirable combination of mechanical properties e.g. high strength and good formability [1]. To protect the steel from corrosion and thus to achieve a long-term structural stability during routine vehicle operation, continuous hot-dip galvanizing is commonly applied, where the steel sheet passes through annealing furnaces before immersion into the zinc bath [1,2]. However, although the oxygen partial pressure level in the commonly used industrial N_2-(5~20 vol%) H_2-xH_2O ($P_{H2O}/P_{H2} = 10^{-4}$ to 10^{-1} [3]) annealing atmosphere is below the thermodynamic onset of wüstite (FeO) formation, it is still sufficient to oxidize alloying elements possessing higher affinity to oxygen such as Mn, Si, Cr and Al.

Surface selective oxidation of the more reactive alloying elements can adversely affect the wettability of the steel substrate during continuous galvanizing in the Zn (Al) bath [4–7]. Besides the chemical composition the morphology of the surface oxides is crucial for the formation of a well-developed Fe2Al5-xZnx inhibition layer. It has been reported that at same coverage of oxides over the substrate, the smaller oxide islands were less detrimental to the reaction kinetics than the larger ones because the growing Fe2Al5 crystals could overgrow the small oxide islands more easily [8]. Moreover, internal selective oxidation especially along grain boundaries induced during annealing process weakens the cohesion between individual grains and causes embrittlement [9]. Mn is an indispensable element in high strength steels and interestingly, its combination with certain alloying elements

leads to a significantly enhanced grain boundary (GB) oxidation [4,9]. Consequently, an in-depth understanding of the selective oxidation of alloying elements is extremely important for a careful design of the annealing processes and composition optimization of high strength steels. Beside the many works on high temperature oxidation of technical alloys possessing complex steel compositions (see e.g. [10,11]), which complicate a clear definition of enhancing effect of certain element combinations, only little is reported on the oxidation properties of well-defined model systems [2,4,9].

Mao et al. [4] carried out oxidation measurements in Fe-Mn steels with various Cr and Si concentrations at 950 °C in a gas mixture of Ar or N_2 with 5 vol.% H_2 and dew points ranging from −45 to 10 °C. The results showed that Fe-Mn-Cr alloys exhibited a similar oxidation mode to that of Fe-Mn alloys and the addition of Si into the Fe-Mn-Cr alloys led to the formation of $(Mn,Fe)_2SiO_4$ both along grain boundaries and inside grains. However, that work mainly addressed the outer scaling and not that much internal selective oxidation. Pourmajidian et al. [2] investigated the external and internal oxidation of 0.1C-6Mn-2Si steels with and without Sn addition after annealing at 963 K for holding time of 60–600 s under oxygen partial pressures ranging from 1.20×10^{-27} to 2.26×10^{-23} atm. The authors claimed that both the external and internal oxidation followed a parabolic rate law and diffusion was expected to be the rate-determining step (in agreement with the model proposed by Wagner [9–12]). However, the overall thicknesses of external selective oxidation on these steels oxidized at the oxygen partial pressure of 7.69×10^{-26} atm was found to be much larger than those at 1.20×10^{-27} and 2.26×10^{-23} atm. That is obviously divergent from the Wagner's internal-external transformation theory according to which at the lowest oxygen partial pressure of 1.20×10^{-27} atm the

external oxides should be the thickest [5]. Auinger et al. [9] studied the selective oxidation behavior of binary and ternary iron-based alloys containing Al, Cr, Mn and Si, and found that pronounced oxide formation along grain boundaries could only be seen in the case of Al, Si or Cr added Fe-Mn alloys. The authors attributed the enhanced GB oxidation of the Fe-Mn-{Si, Al or Cr} alloys to the high redox-flexibility of manganese's valency states and accordingly fast ion transport in the Mn-containing mixed oxide crystal, although no clear experimental evidence was provided.

The underlying mechanism of the selective oxidation especially along grain boundaries during annealing process is still not clear and remains to be revealed. Furthermore, for relatively short-term annealing processes kinetic aspects have to be expected to play an extremely important role. The analytical approach adopted by previous researchers to estimate the kinetics of selective oxidation is based on the extended Wagner internal oxidation theory [9–12] for ternary alloys, which for extended oxidation times shows a parabolic rate law. However, to simplify the model and make analytical solutions possible, the extended Wagner internal oxidation theory also has a number of assumptions [13]. One important assumption is that ternary diffusional interactions are neglected and the oxides of the alloying elements do not form mixed oxides such as spinels. This assumption is obviously not valid for the oxidation of Fe-Mn-{Si, Al or Cr} alloys. As a consequence, the effectiveness of using the extended Wagner's theory in this case and the proposed explanations seem quite questionable. Disagreements between the experimental observations after a short-term exposure under low oxygen partial pressures and the relevant theoretical predictions made by the Wagner and modified Wagner models have been reported by some literature [9,11]. The main problems identified in these works are the limitations of the diffusivity and solubility data as well as the oversimplicity of the model which, for instance, does not take into account mixed oxides.

In this study, mass gain curves of Fe2MnxSi alloys with various Si contents were obtained using a self-made highly sensitive in-situ thermogravimetry, which can significantly reduce the buoyancy and friction effects. Thus much more reliable thermogravimetry signals especially for short term oxidation can be achieved. Chemical and structural features with respect to oxide types and distributions after annealing process were investigated by combining different analytical techniques. The main objectives of this work are to clarify in more detail the oxidation kinetics for the example of Fe-Mn-Si alloys and reveal the effect and underlying mechanism of Si on the selective oxidation of Fe-Mn-based alloys, especially along grain boundaries.

2. Material and methods

Fe2MnxSi alloys, denoting model alloys with 2 wt.% Mn and x wt.% Si, with Si contents of 0, 0.25, 1 and 2 wt.%, were selected as ternary model alloys of high strength steels. The alloys were prepared at the Max-Planck-Institut für Eisenforschung GmbH (MPIE) using vacuum melting technique followed by hot-rolling at ~1200 °C. The alloy sheets were cut into specimens with 15 mm × 10 mm × 2 mm in size. A small hole with a diameter of 1.7 mm was drilled, where the sample could be mounted on the quartz hook of the thermobalance. Prior to exposure, all surfaces of the samples were ground to grit 4000 using SiC papers and polished to a mirror finish using 1 μm diamond paste to minimize the effect of substrate roughness on the surface analysis. All the samples were ultrasonically cleaned in ethanol and dried in a cold nitrogen stream.

Selective oxidation experiments were carried out at 700 °C for 2 h in a self-made highly sensitive thermogravimetry set-up, whose assembly has been described in Ref. [14] in detail. Great care has been taken to reduce the content of oxygen impurities below a limit of 5 ppm. A gas mixture of H_2/H_2O (98.0/2.0, v/v, +18 °C dew point) with a total flow of 30 l h^{-1} and chamber pressure of 40 mbar was employed for all the measurements. The substituting of the inert N_2 gas by vacuum from the

commonly used industrial N_2-(5~20 vol%) H_2-xH_2O annealing atmosphere can significantly enhance the signal-to-noise ratio, due to a dramatically reduced buoyancy effect especially after rapid heating [14]. A fast heating rate of 5 K s^{-1} was employed to eliminate the influence of oxidation during heating. All process parameters e.g. mass gain and measured temperature during exposure were recorded automatically, with data collected every second. The thermogravimetry signal from a pure iron sample prepared using the same procedures and exposed to the same conditions was subtracted from the measurements to eliminate the equipment error. The oxygen solubility in iron for the first 2 h is calculated to be well below the resolution of the technique and hence is negligible in this study. Taking the oxygen solubility reported by Swisher and Turkdogan [15], the expected mass gain by dissolved oxygen for the whole sample of 2 mm thickness and for an oxygen partial pressure of the Fe/FeO equilibrium would be less than 0.0017 mg/cm^2. Of course, the oxygen diffusion depth will be much less for 2 h. For pure iron one would get less than 0.2 mm, i.e. the mass gain for pure iron in 2 h would be less than 0.00034 mg/cm^2. In our case at the much lower oxygen partial pressure used in this work the mass gain would even be significantly lower. Hence, the expected mass gain by dissolved oxygen is neglected here. After the annealing process, the samples were left in the chamber to cool down to room temperature in the flowing gas stream. The oxidation tests for all the alloys were performed in triplicate to ensure repeatability of the experimental results. It is worth noting that the commonly used holding time for industrially relevant annealing process prior to hot dip galvanizing is only several minutes (e.g. ~2 min in ref. [16]). It also needs to emphasized here that the aim for adopting an extended annealing time here is to provide a fundamental understanding of the oxidation mechanism of Fe-Mn-Si alloys during short-term oxidation at low oxidation partial pressure.

Thermodynamic calculations of stable phases were carried out based on alloy composition, oxygen partial pressure and temperature using the FACTSAGE program (using the SGPS database). Phase structures of the oxidized alloys were identified using grazing incidence X-ray diffraction (GIXRD) with incidence angle of 1° and power setup of 40 kV/30 mA (Seifert, GE Sensing & Inspection Technologies GmbH, Germany). Surface and cross-sectional morphologies and chemical compositions of the oxidized samples were investigated by scanning electron microscopy (SEM) and energy-dispersive X-ray spectroscopy (EDX) (FE-SEM, LEO 1550 VP, Zeiss/Oxford Instruments). For better cross-section SEM images, all the alloys were mounted with resin, ground to grit 4000 using SiC papers and polished to a mirror finish using 50 nm SiO_2 suspension. Transmission electron microscopy (TEM) specimen was prepared using the focused ion beam (FIB) technique (FEI Helios Nanolab 600/600i). TEM equipped with an EDX was employed for a more detailed analysis of the microstructure especially along grain boundaries. Elemental analyses were conducted by X-ray photoelectron spectroscopy (XPS, Physical Electronics Quantum 2000 Scanning ESCA Microprobe) with Al Kα excitation (hν = 1,486.6 eV). For depth profiling, the oxidized surfaces of the samples were etched using an argon ion beam of 2.0 kV. Standard carbon contamination (284.6 eV) was adopted for the calibration of binding energy. Peak fitting was performed using the CasaXPS software package.

3. Results and discussion

3.1. Oxidation kinetics

Fig. 1 shows the oxidation kinetics of Fe2MnxSi samples with various Si contents during annealing process. Accurate control of the sample temperature can be achieved, with measured temperature quickly stabilizing at the setting temperature of 700 °C after ~300 s. The thermogravimetry signals for both Fe2Mn1Si and Fe2Mn2Si alloys exhibit a well-pronounced signal-to-noise ratio even at the very initial oxidation stage. Accurate measurements of the oxidation kinetics can
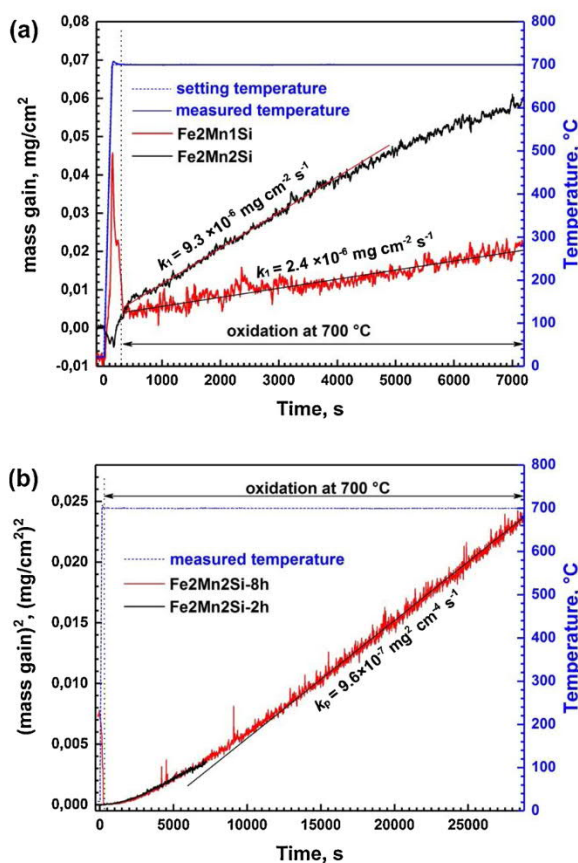
Fig. 1. Oxidation kinetics of Fe2MnxSi samples with various Si contents during heating in the gas mixture of H_2/H_2O ($p(O_2) = 6.5 \times 10^{-25}$ bar at 700 °C).

be acquired almost immediately when the target temperature is reached. Moreover, although the resolution of the thermogravimetry signal is ultra-high with a value of less than $10 \, \mu g \, cm^{-2}$, the mass gain curves of Fe2Mn and Fe2Mn0.25Si alloys remain almost unchanged during the whole measurements, indicating an extremely low oxide growth, and hence are not shown here. It can be seen from Fig. 1a that increasing the Si content in the alloy contributes to a larger mass gain. The kinetic of the Fe2Mn1Si alloy exposed to H_2/H_2O follows a linear growth during the first 2 h oxidation, with a linear rate constant k_l equal to $2.4 \times 10^{-6} \, mg \, cm^{-2} \, s^{-1}$. The kinetics of the Fe2Mn2Si alloy initially also show a linear growth stage, lasting from the very beginning to ~4200 s with a linear rate constant k_l equal to $9.3 \times 10^{-6} \, mg$ $cm^{-2} \, s^{-1}$, followed by rather parabolic behavior (see Fig. 1b). In view of the linear behavior of the mass gain for Fe2Mn1Si and Fe2Mn2Si under low oxidation partial pressure it is proposed that oxygen uptake is the rate determining step for short term oxidation. This is discussed in more detail in section 3.4.

For long term oxidation the kinetics will usually become parabolic, as with depth diffusion will finally be rate determining step. Accordingly, the exposure period was extended to 8 h to see whether the behavior of the parabolic second stage remained constant after further oxidation (Fig. 1b). It is shown that the slope for the Δw^2-t curve (where Δw refers to mass gain and t refers to time) increases with time after ~2 h oxidation, and reaches to a constant value of $9.6 \times 10^{-7} \, mg^2 \, cm^{-4} \, s^{-1}$ after ~3.5 h oxidation. If the growth process would be already fully parabolic at the end of the first two hours, we should see the same parabolic rate continuing also for the following hours. However, for the time between 2 h and 8 h the slope of the Δw^2-t curve is clearly different. Furthermore, we do not see any significant changes in the oxidation morphology between 2 h and 8 h oxidized samples (both on top as well as cross-section SEM analysis does not

reveal any notable changes in morphology, as shown in Figs. 3, 4 and A4, which could explain a change of the parabolic rate. Hence, we conclude that in the first $1-2$ h the growth rate is definitely linear and even at the end of the two hours not fully parabolic yet.

Actually, at low oxygen partial pressures the kinetics of oxygen (or rather water) dissociation and/or the absorption of oxygen into the sample surface should be very low, and thus oxygen uptake is expected to be the rate-limiting step for oxidation at the early stage. An unexpected lower oxygen activity on the sample surface than what is thermodynamically expected has been shown experimentally by Borodin et al. when investigating selective surface oxidation of Fe2Mn alloy using in-situ XPS technique [17]. Since the diffusion lengths of both oxygen and alloying elements into the near-surface regions are virtually short at initial oxidation stage, it is highly likely that element diffusion is not the rate determining step for short term oxidation. It is also worth noting that the repeatability of the thermogravimetry experiments in this work is fairly good, as shown in Fig. 1b.

3.2. Morphology and scale structure

The oxygen partial pressure-temperature phase diagrams for Fe2MnxSi alloys with various Si contents are presented in Figs. A1–3. The thermodynamically stable phases after oxidizing at 700 °C under oxygen partial pressure of 6.5×10^{-25} bar are MnO + α-Fe for Fe2Mn, Mn_2SiO_4 + MnO + α-Fe for Fe2Mn0.25Si and Mn_2SiO_4 + SiO_2 + α-Fe for Fe2Mn1Si and Fe2Mn2Si, respectively. The calculated oxygen partial pressure ($P(O_2) = 6.5 \times 10^{-25}$ bar at 700 °C) is sufficient for the oxidation of alloying elements i.e. Mn and Si, but is below the Fe/FeO equilibrium. Fig. 2 shows the XRD patterns obtained from the Fe2MnxSi alloys with various Si contents after annealing in the gas mixture of H_2/H_2O at 700 °C for 2 h. The oxides formed on the surfaces of the Fe2Mn and Fe2Mn0.25Si alloys are mainly composed of MnO [18], and the oxides for the Fe2Mn1Si and Fe2Mn2Si alloys of Mn_2SiO_4 [19]. Actually, there are also other oxides formed during oxidation, as confirmed by the following observations, which are not detected by XRD. The reason why XRD failed to detect these other oxides is probably because they are amorphous and/or the amount is too small.

Fig. 3 presents the surface morphologies of Fe2MnxSi alloys with various Si contents after annealing in the gas mixture of H_2/H_2O at 700 °C for 2 h. For Fe2Mn, surface oxidation appears as large ridges that outline the alloy grain boundaries, which is ascribed to MnO. The addition of Si to Fe2Mn leads to the formation of metallic Fe nodules on the sample surfaces especially along grain boundaries. For Fe2Mn0.25Si, both MnO (Fe-16.6Mn-14.8O (at.%) for point 1) and metallic Fe appear on grain boundaries, as confirmed by EDX (also by TEM/EDX in Fig. A6); whereas for Fe2Mn1Si and Fe2Mn2Si, the MnO ridges almost disappear completely (100 at.% Fe for points 2 and 3). Meanwhile, surface morphologies become rougher and the sizes of the Fe nodules become larger with the increase in the Si content.

The formation of the external metallic nodules as a consequence of internal oxidation was observed firstly in silver alloys [20] and believed to be caused by deformation phenomena [21,22]. Yet, Schimmel et al. [23] proved the nodule formation to be independent of the loading conditions of the material, referring to the density difference between internal oxides and alloy as the driving force for the local stresses that cause the diffusion of matrix material to the surface. In this work, since the molar volume of all the thermodynamically expected oxides ($27.3 \, cm^3 \, mol^{-1}$ for SiO_2 when amorphous, $50.5 \, cm^3 \, mol^{-1}$ for Mn_2SiO_4 and $13.1 \, cm^3 \, mol^{-1}$ for MnO) is significantly higher than that for Fe ($7.1 \, cm^3 \, mol^{-1}$), the severer selective oxidation for alloys with higher Si leads to larger volume expansion which thus is proposed to be the cause for a more pronounced diffusion of Fe to the upmost surface. Yi et al. [24] reported a similar phenomenon that the internal precipitation of SiO_2 (and alumina) caused ejection of base metal to form surface nodules.

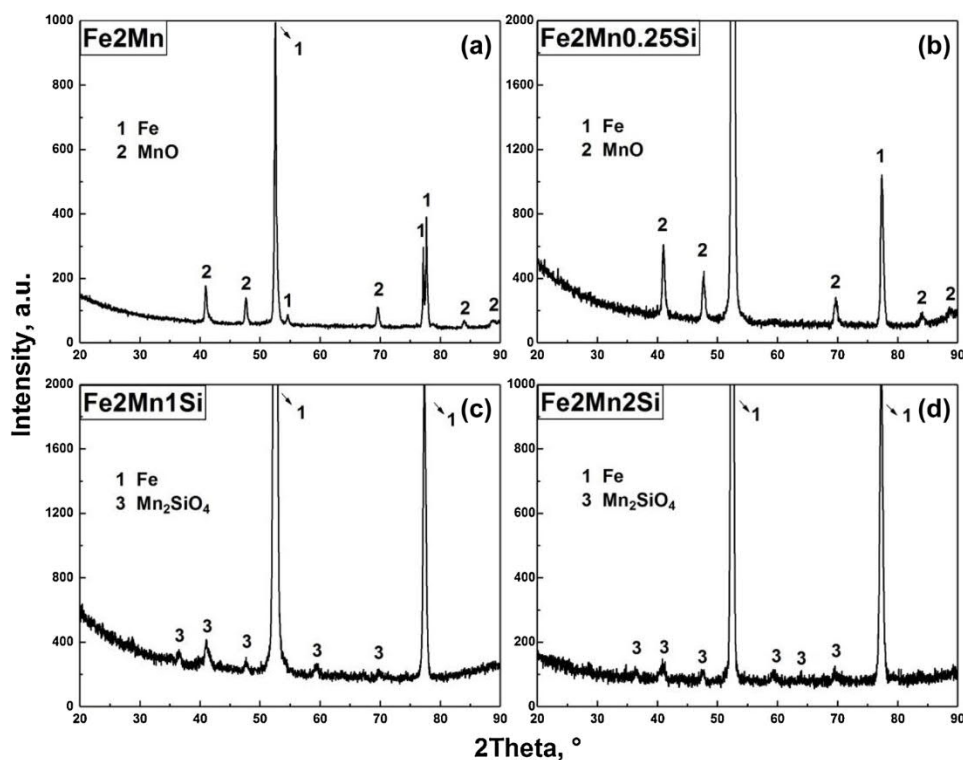Cross-sectional morphologies of Fe2MnxSi alloys with various Si

Fig. 2. XRD patterns of Fe2MnxSi alloys with various Si contents after annealing in the gas mixture of H_2/H_2O at 700 °C for 2 h.

contents after annealing in the gas mixture of H_2/H_2O at 700 °C for 2 h are shown in Fig. 4. Only extremely low amounts of internal MnO particles can be observed for Fe2Mn, all of which are located at the near-surface region encompassing the first ∼ 200 nm below the surface. By comparison, a significantly enhanced internal oxidation especially along grain boundaries occurs for Si-containing alloys. The GB oxidation depth of the alloys increases with Si content, with ∼ 4.7 μm for Fe2Mn0.25Si, ∼ 6.6 μm for Fe2Mn1Si and ∼ 6.8 μm for Fe2Mn2Si, respectively. The cross-section of the oxidized Fe2Mn0.25Si comprises a network of sub-grain boundary oxides reaching as deep as ∼ 1.6 μm below the sample surface, as shown in Fig. 4d. Some of these oxide particles at the grain boundaries are larger than most of the other oxide particles at grain boundaries. These relatively large GB oxides are

attributed to MnO, as clearly illustrated by the EDX mappings in Fig. A6a. As mentioned, when the Si content in the alloy increased from 0.25 wt.% to 1 wt.%, besides the GB oxidation both the depth and the density of the oxides inside grains also increase distinctly. However, the oxidation degree in some grains is markedly lower than that of others, as shown in Fig. 4e, which is probably due to their special crystal orientations. When the Si content further increased from 1 wt.% to 2 wt.%, the depth of the GB oxidation exhibits only a quite limited increase (if at all) and intracrystalline oxidation develops primarily. The line-scan measurement in Fig. 4g shows that Mn is enriched in the outer sub-surface of Fe2Mn2Si, while Si-rich oxides are found in the inner sub-surface and mainly Mn-Si mixed oxides (probably Mn_2SiO_4) in the grain boundaries. According to previous literature, for Fe-Si alloys with
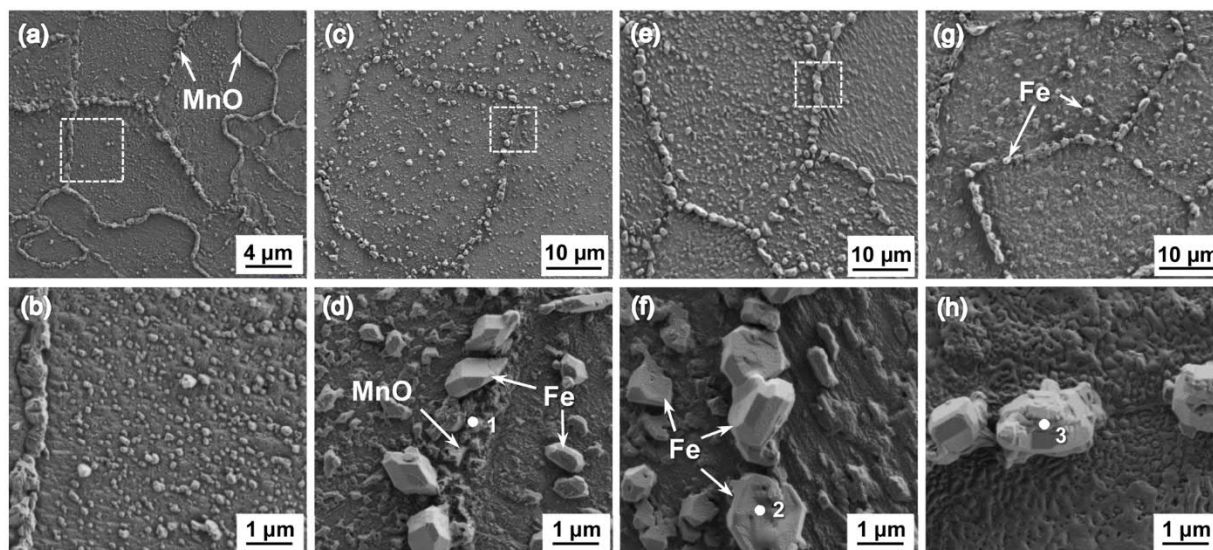

Fig. 3. Surface morphologies of Fe2Mn (a, b), Fe2Mn0.25Si (c, d), Fe2Mn1Si (e, f), Fe2Mn2Si (g, h) alloys after annealing in the gas mixture of H_2/H_2O at 700 °C for 2 h.
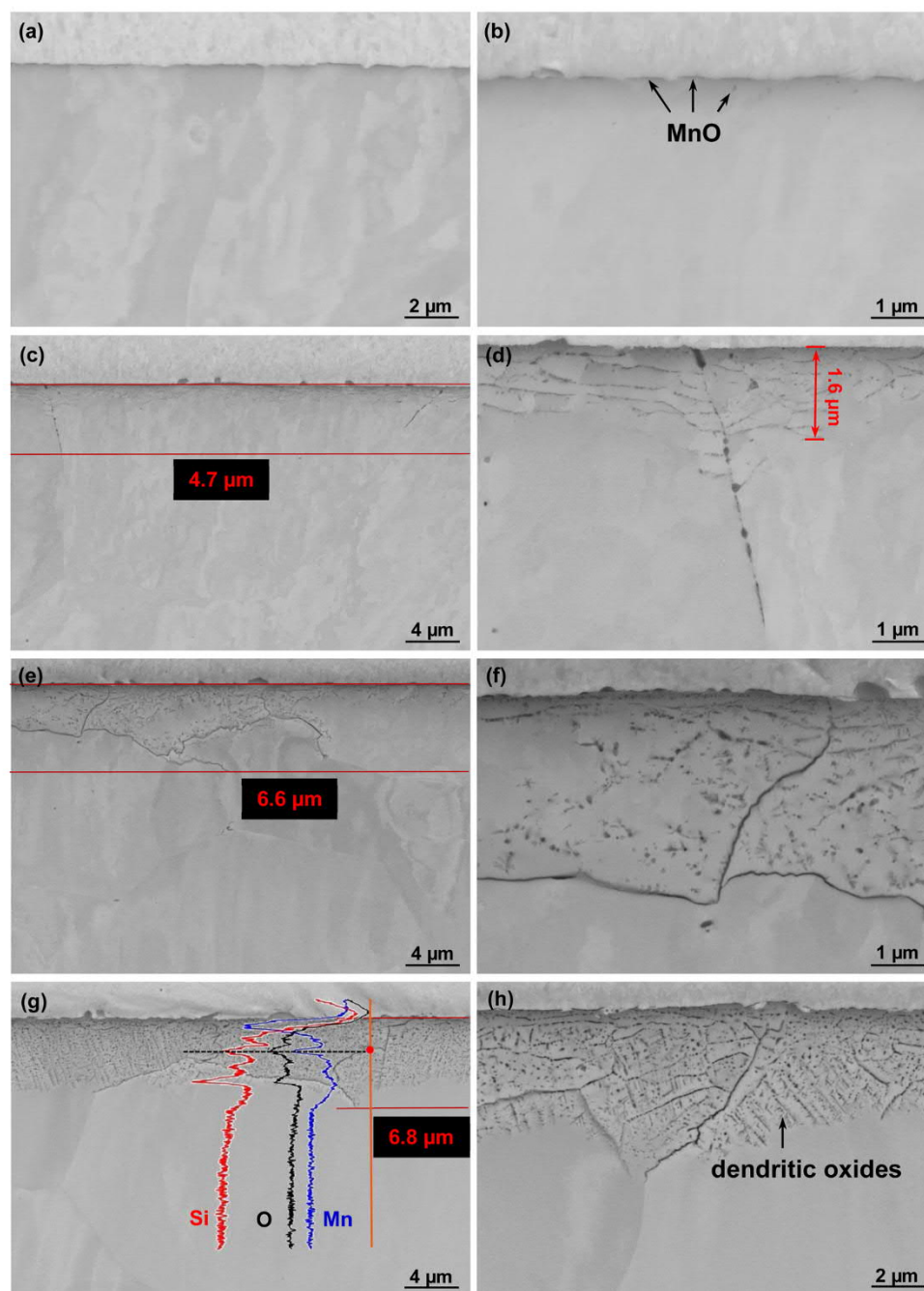
Fig. 4. Cross-sectional morphologies of Fe2Mn (a, b), Fe2Mn0.25Si (c, d), Fe2Mn1Si (e, f) Fe2Mn2Si (g, h) alloys after annealing in the gas mixture of H_2/H_2O with pO_2 of 6.5×10^{-25} bar at 700 °C for 2 h.

silicon contents less than 2 at.%, the shape of the SiO_2 particles formed during selective oxidation was spherical [25], while for alloys with larger silicon contents, dendritic SiO_2 particles started to appear [26]. Accordingly, it is highly likely that the dendritic oxides formed in the inner oxidation zone of Fe2Mn2Si are SiO_2.

Internal precipitation of ternary oxides is a frequently reported phenomenon, and it can be treated theoretically by using the extended versions of Wagner's theory. For instance, Meijering created a model for the calculation of the internal oxidation depth with two precipitate zones assuming immobility of the alloying element and very low product of solubility of its oxides [27]. Using Meijering's model, the calculated oxidation depths for the alloys and annealing conditions used in this work would be 0.51 μm, 0.29 μm and 0.23 μm for Fe2Mn0.25Si, Fe2Mn1Si and Fe2Mn2Si, respectively. The cross sections of the

annealed (Fig. 4) clearly show markedly larger oxidation depths for all samples. The main reason for this huge discrepancy certainly has to be a much higher diffusion coefficient in the alloys investigated here (or rather in the internally oxidized alloys, due to a most likely faster diffusion e.g. at the oxide/metal interfaces) than the one valid for oxygen in pure iron. And since our experimental data show a linear dependence of oxidation on time, the diffusion has to be even that high, that it is not rate determining for roughly the first two hours. This means that we cannot use the diffusion constants for pure alpha iron here and also no model that assumes diffusion as being the rate determining step. Furthermore, the diffusion coefficient of manganese in pure alpha iron at 700 °C (5.6×10^{-13} m^2 s^{-1} [28]) is not negligible compared to that of oxygen (4.5×10^{-12} m^2 s^{-1} [29]). Although the diffusion coefficient for oxygen has to be much higher in our case, Mn enrichment is to be

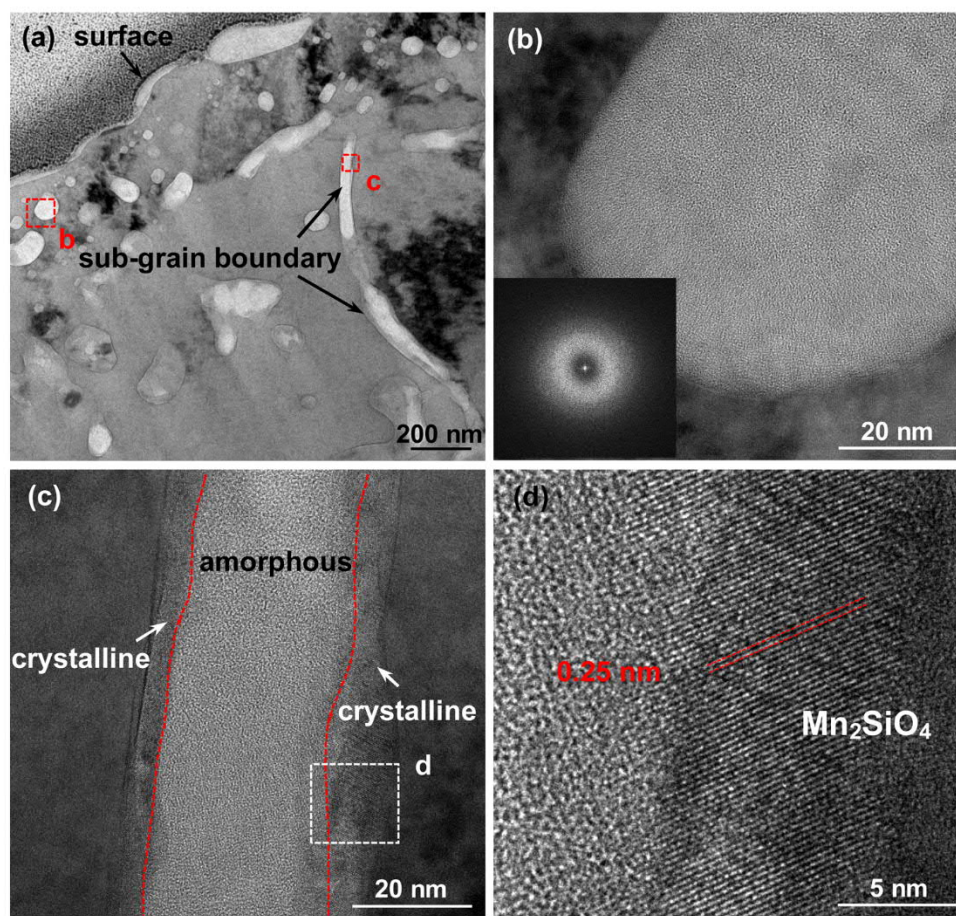**Fig. 5.** TEM image of the cross-section of the Fe2Mn2Si alloy annealed in the gas mixture of H_2/H_2O at 700 °C at an oxygen partial pressure of 6.5×10^{-25} bar for 2 h (a) and zoomed selective areas in the bulk (b) and along the sub-grain boundary (c, d).

expected, which we indeed observe.

A more detailed characterization of the microstructure of Fe2Mn2Si after the annealing process is presented in Fig. 5. It can clearly be seen from the TEM image (Fig. 5a) that interrupted film-like oxides with dozens of nanometers thickness appear at the upmost surface, along with selective internal oxidation both in the bulk and along grain boundaries. The selected oxide particle in the bulk ferrite yields amorphous diffraction ring, indicating that it has an amorphous structure (Fig. 5b Interestingly, although the inner region of the selected sub-grain oxide is also amorphous, its external region adjacent to the matrix becomes crystalline, as illustrated in Fig. 5c and d. The HRTEM image of the external region of the oxide suggests a plane distance of 0.25 nm, which corresponds to the lattice plane (112) of Mn_2SiO_4 phase [19]. The presence of Mn_2SiO_4 coincides with the XRD results.

Fig. 6 displays the TEM cross-sectional micrograph of the outer oxidation region of Fe2Mn2Si after annealing in the gas mixture of H_2/H_2O at 700 °C for 2 h and corresponding mappings of Mn, Si, Fe and O. The surface oxide layer is mainly composed of flat Mn oxides, with trace amounts of Si distributed in the oxides. These external oxides can be probably best ascribed to SiO_2 (and/or Mn_2SiO_4) doped MnO. Meanwhile, the GB oxide network is rich in both Mn and Si, with the two elements relatively evenly distributed in some of the oxides. Interestingly, a group of GB oxides shows a layered structure composed of a Si-rich oxide core and a surrounding Mn-Si mixed oxide shell being identified as SiO_2 and Mn_2SiO_4 respectively, as partially marked by white dotted circles. A similar layered structure can be observed for

some Mn-Si mixed oxides in the bulk, as partially marked by red dotted circles. Besides the Mn-Si mixed oxides a number of SiO_2 particles are also formed inside the grains, as partially marked by pink dotted circles.

Fig. 7 shows the TEM cross-sectional micrograph of the inner oxidation region and corresponding mappings of Mn, Si, Fe and O. The inner GB oxide network also comprises both Mn and Si, while all the particles in the deeper bulk consist of SiO_2 only. The magnified elemental maps for the selected GB oxidation region clearly display the difference in the composition of the oxide from its center to its shell. It is worth noting that such a layered structure of the Mn-Si oxides cannot be observed for Fe2Mn0.25Si, as displayed in Fig. A6, which is in accordance with the phase diagram in Fig. A2 where no SiO_2 should be formed under the conditions of interest.

3.3. Elemental analysis of the oxide scales

The near-surface chemistry of the alloys after annealing process, i.e. especially the oxide at the surface, is extremely important for reactive wetting during the following galvanizing step and might also play an important role in the growth of the internal oxides, if it has an effect on oxygen uptake. Concerning the latter, it is obvious from our results that the oxygen uptake has to increase with the amount of alloying elements, especially silicon. An assumption is that the ternary phase boundary silica/metal/gas phase might enhance the oxygen uptake. Hence, the composition and the quantity of the external oxides is expected to play a role. Also, as long as diffusion is not rate determining,
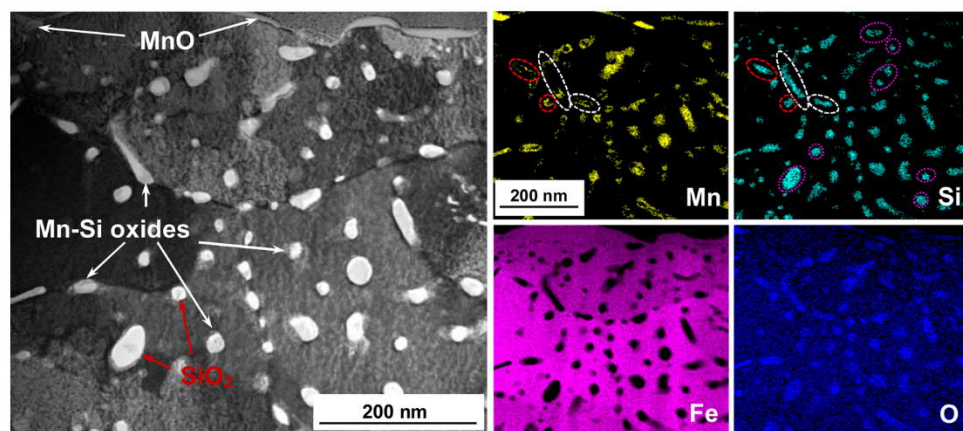
Fig. 6. TEM cross-sectional micrograph of the Fe2Mn2Si alloy (upper part) annealed in the gas mixture of H_2/H_2O with oxygen partial pressure of 6.5×10^{-25} bar at 700 °C for 2 h and corresponding mappings of Mn, Si, Fe and O. Many GB oxides exhibit a layered structure with a Si-rich oxide core and a surrounding Mn-Si mixed oxide shell, as partially marked by white dotted circles. A similar layered structure can be observed also for intracrystalline Mn-Si mixed oxides, as partially marked by red dotted circles. Si-rich oxides are also formed in the bulk, as partially marked by pink dotted circles (For interpretation of the references to colour in this figure legend, the reader is referred to the web version of this article).
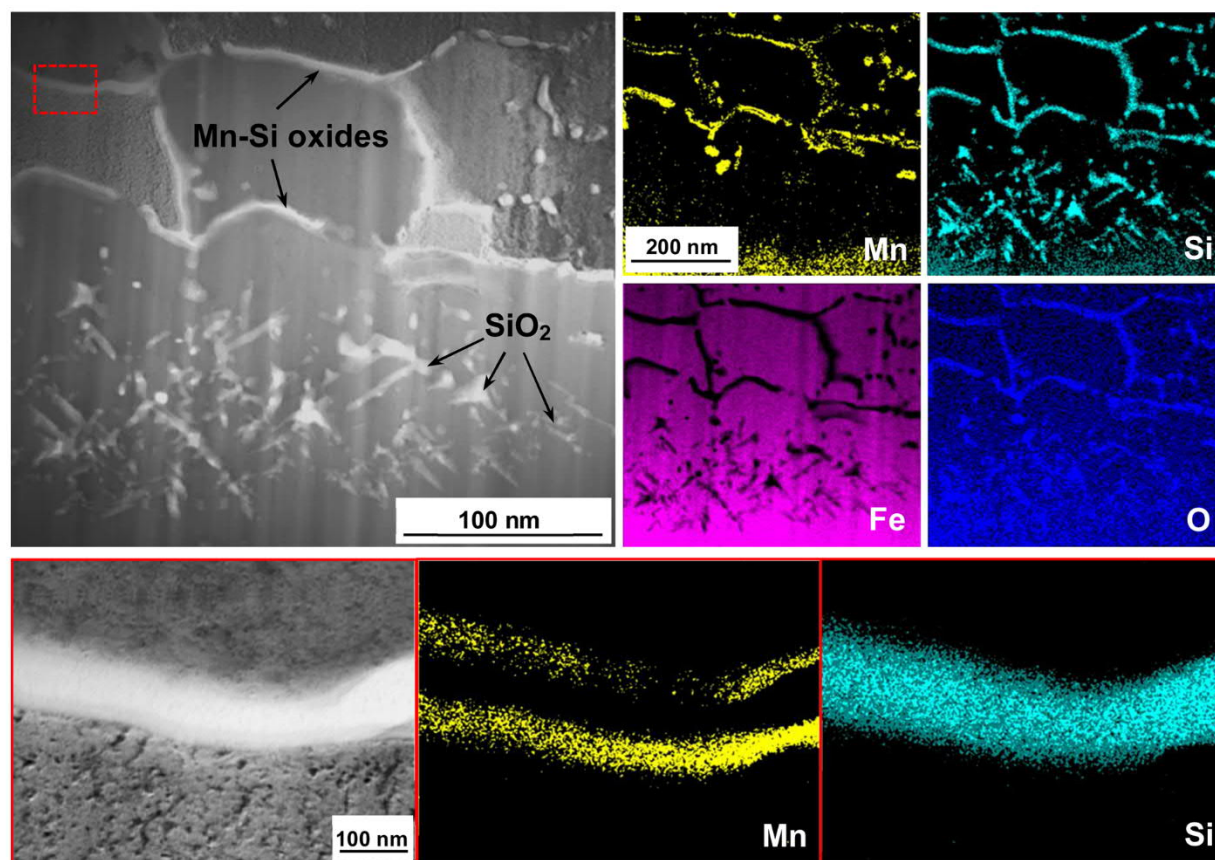

Fig. 7. TEM cross-sectional micrograph of the Fe2Mn2Si alloy (inner part) annealed in the gas mixture of H_2/H_2O with oxygen partial pressure of 6.5×10^{-25} bar at 700 °C for 2 h and corresponding mappings of Mn, Si, Fe and O.

all O that enter the alloy at the surface will quickly diffuse to the oxidation front. With the uptake being rate determining this means that the concentration just below the surface should be well below the thermodynamically expected oxygen concentration in equilibrium with the gas phase and this is expected to be the more the case the higher the concentration of alloying element. As the uptake can be expected to be proportional to the difference in chemical potential of oxygen on the surface and just below the surface, this lower O concentration and the correlated lower chemical potential should lead to a higher uptake rate. Thus, the composition and the quantity of the internal oxides is also proposed to play a role. For these reasons, the chemical states of the

oxidized alloys were analyzed by means of XPS to obtain information about the composition and distribution of the oxides formed at the surface and internally during the annealing process.

Fig. 8 shows the XPS sputtering depth profiles of Mn $2p_{3/2}$, Si 2p and Fe $2p_{3/2}$ for the Fe2Mn0.25Si alloy annealed in the gas mixture of H_2/H_2O with an oxygen partial pressure of 6.5×10^{-25} bar at 700 °C for 2 h. For the whole sputtering process (duration of 2286s, depth about 1.1 μm), all the spectra of Mn $2p_{3/2}$ can be fitted into two components, MnO at a binding energy of 640.5 eV [30] and Mn_2SiO_4 at binding energies ranging from 641.7–642.0 eV [31,32] (Fig. 8a). Although the Mn_2SiO_4 concentration seems even larger than that of MnO, as can be
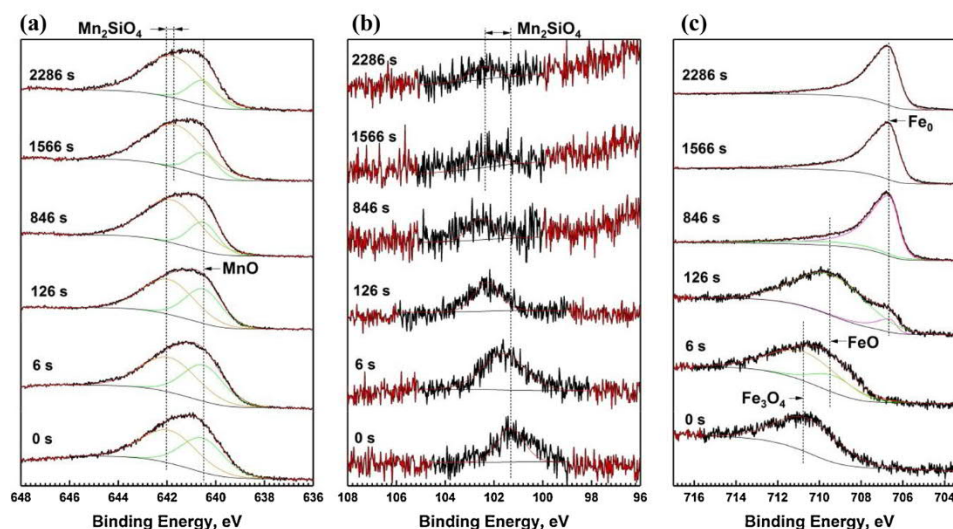
Fig. 8. XPS sputtering depth profiles of Mn $2p_{3/2}$ (a), Si 2p (b) and Fe $2p_{3/2}$ (c) for the Fe2Mn0.25Si alloy annealed in the gas mixture of H_2/H_2O at 700 °C for 2 h.

derived by comparing their peak areas, no Mn_2SiO_4 can be detected by XRD analysis. This indicates that quite an amount of Mn_2SiO_4 exists as amorphous form. The variation of the adjacent chemical state e.g. the change in the proportions of the non-bridging oxygen atoms would result in the slightly shift of the Mn $2p_{3/2}$ binding energy in the amorphous Mn_2SiO_4. The chemical shift in the core level binding energy for amorphous phases is an intensely discussed observation [33–35]. It is also worth noticing that although the binding energies of Mn_2O_3 and Mn_3O_4 reported in some literature may also fall in the interval of $641.7 \sim 642.0$ eV [30,36], they are unlikely to form in this case as the oxygen partial pressure under conditions of interest is several orders of magnitude lower than the onset of the MnO/Mn_3O_4 equilibrium (not to mention the Mn_3O_4/Mn_2O_3 equilibrium). Meanwhile, the peak area ratios of Mn_2SiO_4 to MnO increase with sputtering time, indicating that the fraction of MnO decreases whereas the fraction of Mn_2SiO_4 increases from the surface to the matrix. The formation of Mn_2SiO_4 can be further verified by studying the core level spectra of Si 2p.

It is shown in Fig. 8b that the Si 2p spectra can be fitted into one peak at binding energies ranging from 101.3–102.2 eV. Again, the shift

of the Si 2p binding energy is ascribed to the variation of the adjacent chemical state of the amorphous Mn_2SiO_4. For the Fe $2p_{3/2}$ spectra, a single Fe $2p_{3/2}$ peak with binding energy at ~710.7 eV is recorded at the upmost surface, which is ascribed to Fe_3O_4 [37]. The Fe $2p_{3/2}$ spectrum after 6 s sputtering has two peaks at binding energies of ~710.7 eV and ~709.4 eV, corresponding to Fe_3O_4 and FeO [38], respectively. After 126 s sputtering, no Fe_3O_4 signal can be observed any more, while metallic Fe with binding energy peak at 706.9 eV [39] begins to appear alongside FeO. The amount of FeO is negligible after 846 s sputtering. Only metallic Fe can be detected after further sputtering. The Fe oxides are actually formed during cooling process, because Fe is thermodynamically expected to be oxidized at lower temperature only (roughly below 300 °C) and remain metallic at higher temperatures, as shown in Fig. A2. The extremely thin Fe oxide layer further reflects the stability of metallic Fe at the experimental temperature of 700 °C.

Fig. 9 shows the XPS sputtering depth profiles of Mn $2p_{3/2}$, Si 2p and Fe $2p_{3/2}$ for the Fe2Mn1Si alloy annealed in the gas mixture of H_2/H_2O with an oxygen partial pressure of 6.5×10^{-25} bar at 700 °C for 2 h. As can be seen Mn_2SiO_4 appears during the sputtering process (duration of
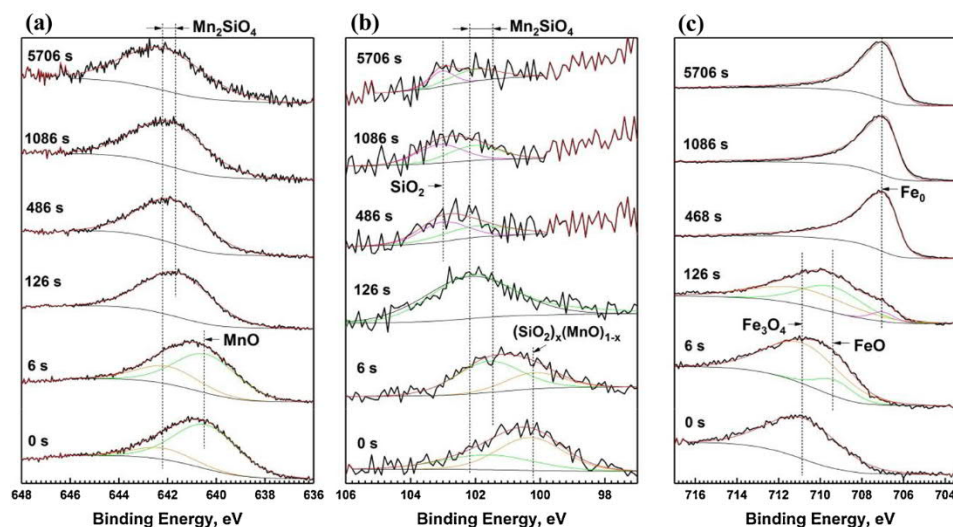

Fig. 9. XPS sputtering depth profiles of Mn $2p_{3/2}$ (a), Si 2p (b) and Fe $2p_{3/2}$ (c) for the Fe2Mn1Si alloy annealed in the gas mixture of H_2/H_2O at 700 °C for 2 h.

5706 s), with binding energies ranging from 641.7–642.2 eV for the Mn $2p_{3/2}$ spectra (Fig. 9a) and from 101.3–102.2 eV for the Si 2p spectra (Fig. 9b). Except for the Mn_2SiO_4 peak, also the MnO peak with binding energy at 640.5 eV appears both on the upmost surface and after 6 s sputtering, but disappears after 126 s sputtering, as shown in Fig. 9a.

For the Si 2p spectra (Fig. 9b), a peak with binding energy at ~100.2 eV can be observed accompanied with the Mn_2SiO_4 peak before 126 s sputtering, probably corresponding to SiO_2 which embedded in the outer MnO. After 486 s sputtering, the $(SiO_2)_x(MnO)_{1-x}$ peak completely disappears and a peak with binding energy at 103.0 eV begins to appear, which is identified as SiO_2 [40]. The downward shift of the Si 2p binding energy for SiO_2 embedded in other amorphous oxides has also been reported previously [34,35]. Mekki et al. [34] studied the XPS spectra of a series of $(SiO_2)_{0.7-x}(Na_2O)_{0.3}(Fe_2O_3)_x$ ($0 \leq x \leq 0.18$) glasses. The results showed that the Si 2p peaks shifted to lower binding energies as more Fe was substituted for Si into the glass and a Si 2p peak with binding energy at ~101.1 eV could be observed when x equaled to 0.18. It is foreseeable that a further increase in the x value would lead to a further downward shift of the Si 2p binding energy. Veal et al. [35] also found a similar shift to lower binding energy for the Si 2p level when studying the Na_2O-CaO-SiO_2 system and the authors attributed the downward shift to the Si atoms that bonded to non-bridging oxygen atoms. The suitability to ascribe the Si 2p peak at ~100.2 eV to $(SiO_2)_x$ $(MnO)_{1-x}$ can be strengthened by its appearance at the same sputtering time as MnO (Fig. 9a).

It is shown in Fig. 9c that the $Fe2p_{3/2}$ spectra of Fe2Mn1Si are quite similar to those of Fe2Mn0.25Si. A single peak with binding energy at ~710.7 eV appears at the upmost surface, corresponding to Fe_3O_4. The spectrum obtained after 6 s sputter reveals the presence of Fe_3O_4 and FeO. After 126 s sputtering, metallic Fe signals begin to appear. After 486 s sputtering, Fe_3O_4 and FeO signals disappear completely, and only metallic Fe information can be observed. Actually, Fe_2SiO_4 is also supposed to form during cooling, based on thermodynamic calculation. However, since the Si 2p and Fe $2p_{3/2}$ binding energies of Fe_2SiO_4 [41] resemble those of Mn_2SiO_4 and FeO, respectively, it is difficult to distinguish it.

The XPS spectra of Fe2Mn2Si annealed at 700 °C for 2 h are quite similar to those of Fe2Mn1Si, but exhibit a deeper MnO and $(SiO_2)_x$ $(MnO)_{1-x}$, as displayed in Fig. 10. The increase in the thickness of the MnO surface layer for Fe2Mn2Si is probably because higher tensile stress caused by severer internal oxidation boosts the outward diffusion of Mn and hence an enhanced accumulation of Mn at the near-surface.

The appearance of the Si 2p peak at ~100.2 eV at the same sputtering time as when MnO appears further confirmed the suitability to attribute this peak to $(SiO_2)_x(MnO)_{1-x}$.

It is worth mentioning that the formation of MnO is thermodynamically not expected for Fe2Mn1Si and Fe2Mn2Si under the conditions of the experiment, as shown in the oxygen partial pressure-temperature phase diagram in Fig. A3. However, the accumulation of Mn and the relatively high Mn/Si ratio at the near-surface thermodynamically make it possible to form external MnO during the annealing process. It is known that the diffusion coefficients of both Mn and Si are significantly larger than that of Fe in ferrite [28,42,43]. Accordingly, driven by the oxygen potential gradient, both Mn and Si can diffuse outwards with a quite high rate. Since the oxygen partial pressure required for forming SiO_2 is several orders of magnitude lower than that for MnO, Si will be oxidized during its way to the surface where the oxygen activity is high enough to form SiO_2, retarding the accumulation of Si in the external regions. The line-scan measurement shown in Fig. 4g and the elemental maps shown in Fig. 6 also indicate the enrichment of Mn at the external surface, both of which are consistent with the XPS depth profile results.

3.4. Discussion

The above experimental results show that the addition of Si into the Fe2Mn alloys significantly promotes the selective internal oxidation especially along grain boundaries, and the overall oxidation rate significantly increases with the Si content. Contrary to the general belief that diffusion is the rate-determining step even for relative short-term annealing process of 60 s~2 h under low oxidation pressures [1,2,9], our highly sensitive in-situ thermogravimetry measurements reveal that both the Fe2Mn1Si and Fe2Mn2Si alloys (at least initially) follow linear growth and thus oxygen uptake is probably the rate-controlling step. As is well known, the initial oxidation process can be divided into five steps: 1) reactant gas molecules approach the surface and 2) become adsorbed there and the adsorbed molecules then dissociate to form adsorbed oxygen, which eventually gets absorbed into the metal, 3) the absorbed oxygen diffuses in the metal where it 4) reacts with alloying elements to form an oxide nucleus which then 5) further growth alongside with further oxide nuclei formation. The first two steps refer to gas mass transport and oxygen uptake, respectively. If step 1) was the slowest process, all alloys investigated here should exhibit the same oxidation kinetics. This is definitely not the case in this study. Step 3) is
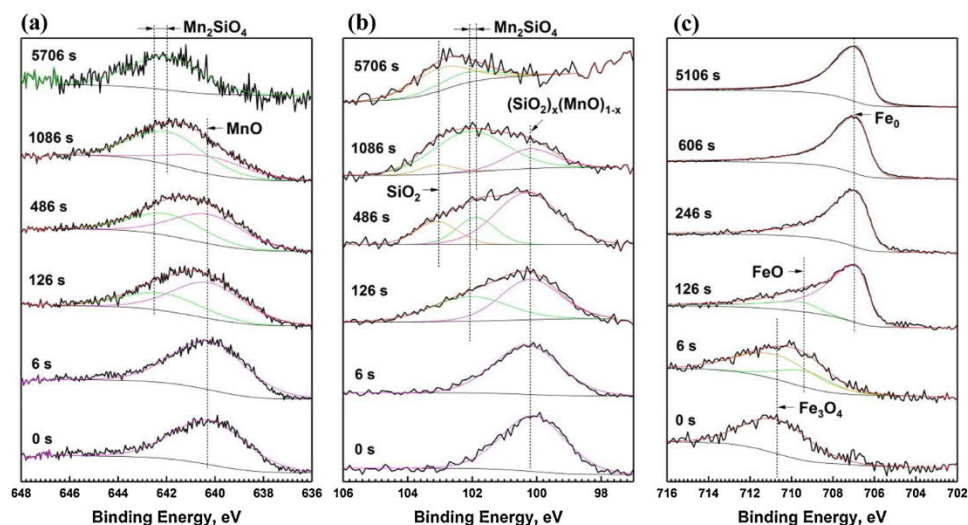

Fig. 10. XPS sputtering depth profiles of Mn $2p_{3/2}$ (a), Si 2p (b) and Fe $2p_{3/2}$ (c) for the Fe2Mn2Si alloy annealed in the gas mixture of H_2/H_2O at 700 °C for 2 h.
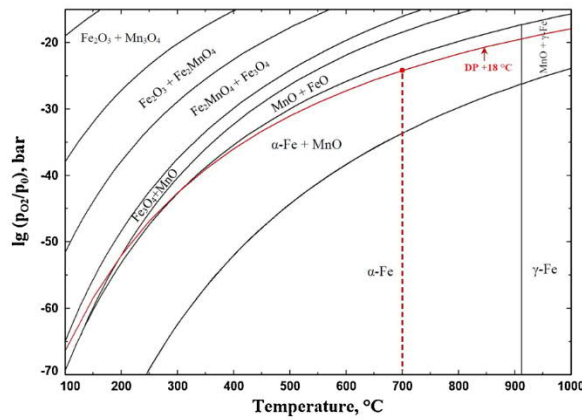
Fig. A1. Oxygen partial pressure-temperature phase diagram for Fe2Mn (where $p_0 = 1$ bar).
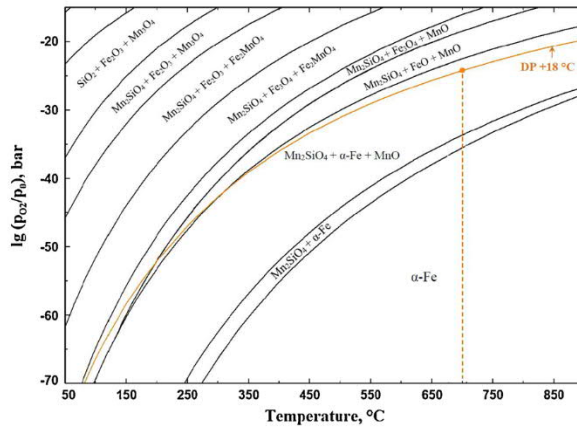

Fig. A2. Oxygen partial pressure-temperature phase diagram for Fe2Mn0.25Si.
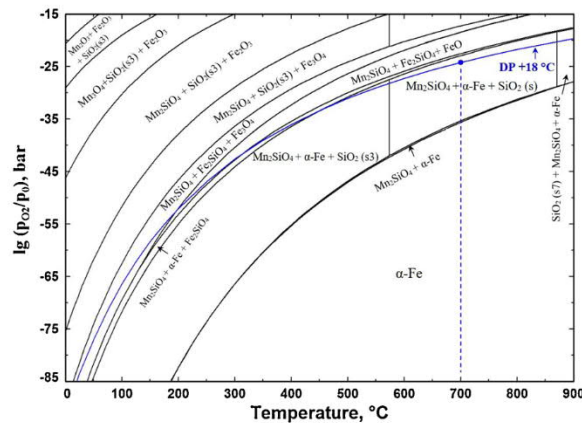

Fig. A3. Oxygen partial pressure-temperature phase diagram for Fe2Mn1Si and Fe2Mn2Si (where SiO_2 (s) = beta-quartz, SiO_2 (s3) = alpha-quartz, SiO_2 (s7) = tridymite).

the rate-limiting step normally in the case of a parabolic mass gain. Especially step 4) could possibly also cause linear kinetics, but a low nucleation rate alone would also mainly cause a much deeper internal oxidation than to be expected (because only little oxygen is consumed while diffusing further into the bulk), which quickly should result in diffusion-controlled transport. Hence, step 2) is definitely the most likely rate-determining step for the linear growth of the alloys here. Although the mass gain signals of Fe2Mn and Fe2Mn0.25Si are too low

to be detected, oxygen uptake is also supposed to be the rate-limiting step for the selective oxidation of the two alloys due to the quite similar alloy compositions and exactly the same annealing atmosphere as those for Fe2Mn1Si and Fe2Mn2Si.

For Fe2Mn external MnO appears as large ridges that outline the alloy grain boundaries, whereas only little internal oxidation can be observed after the annealing process. This can be attributed to fast Mn outwards diffusion along the surface grain boundaries. For
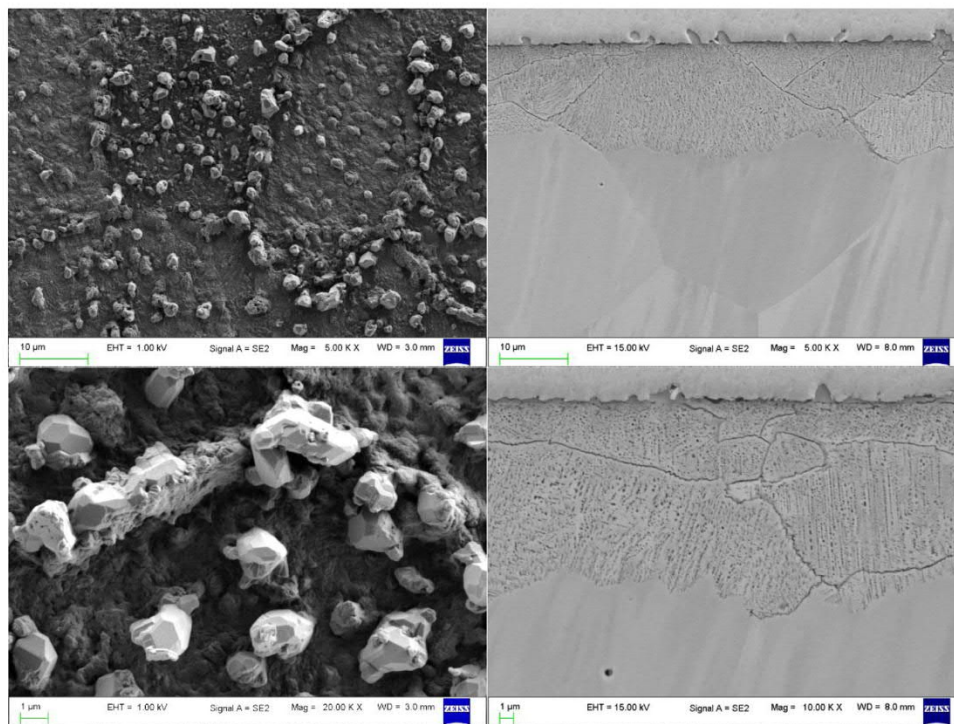
Fig. A4. SEM morphologies of the Fe2Mn2Si alloys after annealing in the gas mixture of H_2/H_2O at 700 °C at an oxygen partial pressure of 6.5×10^{-25} bar for 8 h.

Fe2Mn0.25Si selective internal oxidation is mainly present along grain boundaries as well as sub-grain boundaries, both of which mainly consist of Mn_2SiO_4, alongside some relatively large GB oxides corresponding to MnO. For Fe2Mn1Si, the oxidation depth and the oxide density both in the bulk and along grain boundaries increase remarkably. A further increase in the Si content from 1 wt.% to 2 wt.% has no obvious effect on the oxidation depth in general, but notably enhances the oxide density inside the grains. This may indicate that nucleation of silica at low Si content is easier at the grain boundaries than inside the grains, but is facilitated inside the grains by higher Si contents.

According to the TEM observations (see Fig. 7), SiO_2 is supposed to be the first oxide to form at the grain boundaries, followed by the formation of the Mn_2SiO_4 shell, which clearly demonstrates the role of the silica for nucleation of Mn oxides. Seyed-Mousavi et al. [1] also found a similar structure with SiO_2 as the core and $MnSiO_3$ as the shell when heat-treating Fe-0.1C-2Mn-1.3Si (wt.%) under low oxygen partial pressures. The authors claimed that the preferential formation of SiO_2 was because of its higher thermodynamic stability in comparison with MnO and Mn-silicate species and a near-zero solubility product in ferrite in comparison with MnO (with solubility products of 11.22 $(ppm)^2$ for MnO [44] and 7.2×10^{-5} $(ppm)^3$ for SiO_2 [44], respectively). However, it seems that neither of the two reasons proposed by the authors is convincing. A phase with the highest thermodynamic stability does not mean that it would form in the first place. Besides thermodynamic factors kinetics play an extremely important role for the nucleation and growth of phases, and the preferential formation of metastable phases with relatively low Gibbs free energy before the final stable phases often occurs during solid-solid phase transformations to reduce the phase transition resistance. Additionally, the solubility product of Mn-silicate species in ferrite (4.8×10^{-5} $(ppm)^7$ for Mn_2SiO_4 [45]) is even more negligible than that of SiO_2. The preferential formation of SiO_2 is most likely because the oxygen pressure for the Si/SiO_2 equilibrium (2.9×10^{-39} bar at 700 °C) is significantly lower than that required for forming MnO (4.5×10^{-33} bar at 700 °C) and Mn-silicate species and accordingly SiO_2 starts growing first as soon as the oxygen activity in the alloy reaches to the onset of the Si/SiO_2 equilibrium. With extending the oxidation time, the oxygen activity in a certain position increases to values that are high enough for the formation of Mn-silicate species, i.e. mainly Mn_2SiO_4 in this work, and Mn_2SiO_4 begins to appear subsequently. It has been widely acknowledged that nucleation tends to occur on defect sites such as oxide particles, grain boundaries and other heterogeneities to lower the critical nucleation energy [46]. The easier subsequent formation of MnO and mainly Mn_2SiO_4 on the SiO_2 substrate may probably also be attributed to the similar crystal structures of SiO_2 [47] and Mn_2SiO_4 [19] in both of which each silicon atom is covalently bonded in a tetrahedral manner to 4 oxygen atoms and thus a further reduced surface energy barrier for the nucleation of Mn_2SiO_4 on the initially formed SiO_2 phase. The original SiO_2 core may be gradually transformed into Mn_2SiO_4 with time, which could be verified by the even distribution of Mn and Si in some Mn_2SiO_4 oxides (Fig. 6). As for Fe2Mn0.25Si thermodynamically no SiO_2 should be formed, it is maybe not surprising that the core-shell structure of the Mn-Si oxides was not captured in this work. But there still exists a possibility that the SiO_2 seed are formed transitorily, which may in turn serve as nucleation site for Mn_2SiO_4. Interestingly, a layered structure composed of a Mn_2SiO_4 core and a MnO shell can be observed in Fig. A6, which further indicates that the preferentially formed oxide facilitates the subsequent formation of the more noble one (thermodynamically onset of the oxygen partial pressure: $SiO_2 < Mn_2SiO_4 < MnO$).

It is worth noting again that oxides have a tendency to form along grain boundaries. One reason could be an overall higher oxygen activity at the grain boundaries than in the bulk matrix at the same depth from the surface. Another one certainly is that grain boundaries in comparison with the bulk matrix exhibit larger energy, structural and constituent fluctuations which are beneficial both for the nucleation and growth of new phases. It should be pointed out that besides alloying

elements and annealing parameters, surface machining process and surface roughness of alloys also play a role in the morphology, thickness and distribution of the external oxides after annealing process. The samples used in this work were all polished to a mirror finish to largely remove the processing stress and hence the difference between the surface energies of the grain boundary and the bulk can be highlighted. Actually, we found that external oxides were more evenly distributed on the sample surface for Fe2Mn with relatively large surface roughness.

As mentioned above, the external oxides play an important role in the hot-dip galvanizing process where the external oxides adversely affect the wettability of the steel in the zinc bath. However, in how far our results can provide information on the hot-dip galvanizing behavior is unclear, as the time scale for recrystallisation prior to hot-dip galvanizing is much shorter. Noticeably again, the general picture of the annealing process before galvanizing of alloys is based on the Wagner's internal-external transformation theory, i.e., external oxidation at low dew point whereas internal oxidation at high dew point [5]. This theory is definitely applicable in many cases, but for alloys with relatively high amounts of certain alloying elements this simplified Wagner theory often exhibits large divergence from the experimental observations [2]. Furthermore, the external oxides are certainly important for oxygen uptake: obviously there is an enhanced uptake rate with the increase in the Si content. A small addition of Si can eliminate the external ridge-like MnO oxides, which is probably beneficial for the subsequent galvanizing process, but further increase in Si results in an enhanced external oxidation even again by MnO, most likely due to stress promoted Mn outwards diffusion. Concerning oxygen uptake, two possible explanations for the enhanced oxygen uptake with enhanced silicon content might be the increase in the ternary phase boundary oxide/metal matrix/gas phase (and also changes of its composition) as well as the higher difference in chemical potential of oxygen on the surface and just below the surface.

4. Conclusions

Selective oxidation of Fe2MnxSi alloys with various Si contents formed during annealing at 700 °C at an oxygen partial pressure of $p(O_2) = 6.5 \times 10^{-25}$ bar (adjusted by a H_2/H_2O gas mixture) for 2 h has been investigated. The oxidation kinetics of the Fe2MnxSi alloys with various Si contents followed linear growth, indicating that oxygen uptake was probably 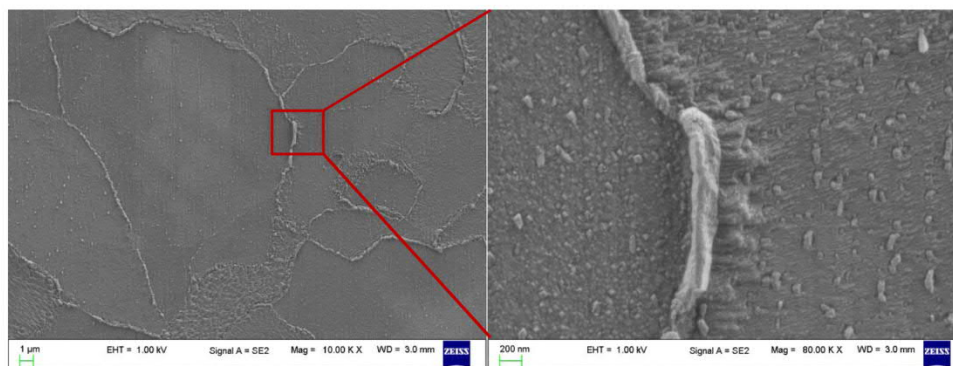the rate-determining step for short-term oxidation. For Fe2Mn, selective oxidation of Mn took place mainly at the surface, forming ridge-like MnO presented along the surface grain boundaries. The addition of Si into Fe2Mn, even at the very small concentration of 0.25 %Si, eliminated the formation of the external ridge-like MnO and tremendously accelerated the internal oxidation of the alloys especially along the grain boundaries. The grain boundaries for the Si-containing alloys were mainly composed of Mn_2SiO_4, with some relatively large MnO particles also for Fe2Mn0.25Si. The depth and the density of the oxides both in the bulk and along the grain boundaries increased with the Si content, with more oxides corresponding to Mn_2SiO_4 and SiO_2 observed inside the grains. The intracrystalline Mn_2SiO_4 mainly exhibited a structure with an outer Mn_2SiO_4 shell embracing a SiO_2 core as that along the grain boundaries for Fe2Mn2Si. Some MnO was also formed on the upmost surfaces of Fe2Mn1Si and Fe2Mn2Si, although thermodynamically not expected, however, only as extremely thin layers.

Data availability

The raw/processed data required to reproduce these findings cannot be shared at this time due to legal or ethical reasons.

CRediT authorship contribution statement

Declaration of Competing Interest

The authors declare that they have no known competing financial interests or personal relationships that could have appeared to influence the work reported in this paper.

Acknowledgement

Appendix

Fig. A5. SEM morphologies of the Fe2Mn alloys after annealing in the gas mixture of H_2/H_2O at 700 °C at an oxygen partial pressure of 6.5×10^{-25} bar for 3 min. The external ridge-like MnO is quite obvious after 3 min exposure, which is close to the time scale for recrystallisation prior to hot-dip galvanizing.
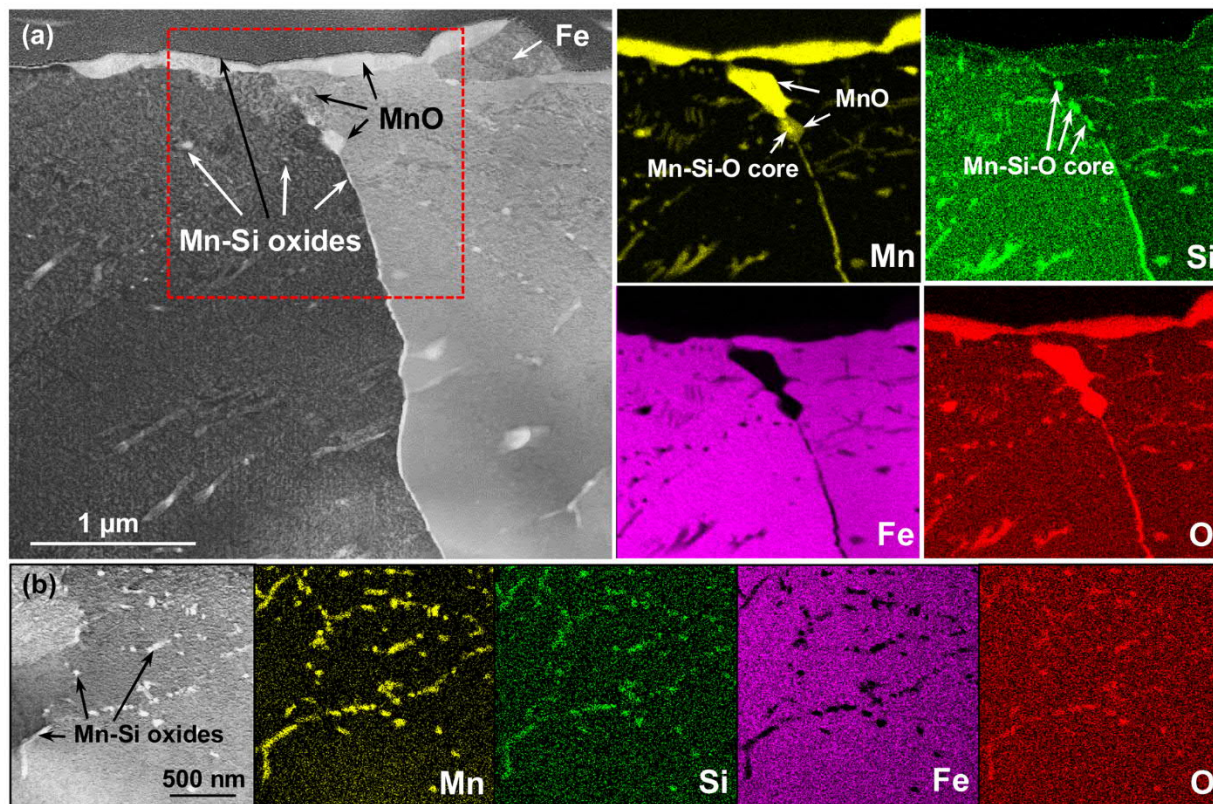
Fig. A6. TEM cross-sectional micrograph of the Fe2Mn0.25Si alloy annealed in the gas mixture of H2/H2O with oxygen partial pressure of 6.5×10^{-25} bar at 700 °C for 2 h and corresponding mappings of Mn, Si, Fe and O. (b) illustrates the region near the oxidation front.

References

[1] J. Seyed Mousavi, J.R. McDermid, Eff ;ect of dew point on the reactive wetting of a C-2Mn-1.3Si (wt%) advanced high strength steel during continuous galvanizing, Surf. Coat. Tech. 351 (2018) 11–20, https://doi.org/10.1016/j.surfcoat.2018.06.060.

[2] M. Pourmajidian, B. Langelier, J.R. McDermid, Effect of process atmosphere dew point and tin addition on oxide morphology and growth for a medium-Mn third generation advanced steel during intercritical annealing, Metall. Mater. Trans. A 49A (2018) 5561–5573, https://doi.org/10.1007/s11661-018-4855-1.

[3] C.R. Shastry, J.A. Rotole, and T.W. Kaiser: Galvatech '07, The Iron and Steel Institute of Japan, Japan, pp. 403-408.

[4] W.C. Mao, R.W.A. Hendrikx, W.G. Sloof, Prediction of oxide phases formed upon internal oxidation of advanced high-strength steels, Oxid. Met. 89 (2018) 531–549, https://doi.org/10.1007/s11085-017-9815-4.

[5] L. Cho, S.J. Lee, M.S. Kim, Y.H. Kim, B.C. De Cooman, Influence of gas atmosphere dew point on the selective oxidation and the reactive wetting during hot dip galvanizing of CMnSi TRIP steel, Metall. Mater. Trans. A 44A (2013) 362–371, https://doi.org/10.1007/s11661-012-1392-1.

[6] R. Sagl, A. Jarosik, D. Stifter, G. Angeli, The role of surface oxides on annealed high-strength steels in hot-dip galvanizing, Corros. Sci. 70 (2013) 268–275, https://doi.org/10.1016/j.corsci.2013.01.039.

[7] H.C. Liu, F. Li, W. Shi, S. Swaminathan, Y.L. He, M. Rohwerder, L. Li, Challenges in hot-dip galvanizing of high strength dual phase steel: surface selective oxidation and mechanical property degradation, Surf. Coat. Technol. 206 (2012) 3428–3436, https://doi.org/10.1016/j.surfcoat.2012.02.001.

[8] S. Frenznick, S. Swaminathan, M. Stratmann, M. Rohwerder, A novel approach to determine high temperature wettability and interfacial reactions in liquid metal/solid interface, J. Mater. Sci. 45 (2010) 2106–2111, https://doi.org/10.1007/s10853-009-4147-7.

[9] M. Auinger, V.G. Praig, B. Linder, H. Danninger, Grain boundary oxidation in iron-based alloys, investigated by ^{18}O enriched water vapour - the effect of mixed oxides in binary and ternary Fe-{Al, Cr, Mn, si} systems, Corros. Sci. 96 (2015) 133–143, https://doi.org/10.1016/j.corsci.2015.04.009.

[10] Z.T. Zhang, I.R. Sohn, F.S. Pettit, G.H. Meier, S. Sridhar, Effect of alloying elements, water vapor content, and temperature on the oxidation of interstitial-free steels, Metall. Mater. Trans. B 40 (2009) 550–566, https://doi.org/10.1007/s11663-009-9238-y.

[11] S.H. Ham, C. Carteret, J. Angulo, G. Fricout, Relation between emissivity evolution during annealing and selective oxidation of TRIP steel, Corros. Sci. 132 (2018) 185–193, https://doi.org/10.1016/j.corsci.2017.12.032.

[12] W.C. Mao, Y. Ma, W.G. Sloof, Internal oxidation of Fe-Mn-Cr steels, simulations and experiments, Oxid. Met. 90 (2018) 237–253, https://doi.org/10.1007/s11085-018-9836-7.

[13] F. Gesmundo, Y. Niu, the internal oxidation of ternary alloys I: the single oxidation of the most-reactive component under low oxidant pressures, Oxid. Met. 60 (2003) 347–370, https://doi.org/10.1023/A:1027398104508.

[14] M. Auinger, A. Vogel, D. Vogel, M. Rohwerder, Early stages of oxidation observed by in situ thermogravimetry in low pressure atmospheres, Corros. Sci. 86 (2014) 183–188, https://doi.org/10.1016/j.corsci.2014.05.010.

[15] J.H. Swisher, E.T. Turkdogan, Solubility, permeability, and diffusivity of oxygen in solid iron, T. Metall. Soc. Aime 239 (1968) 426–431.

[16] H.C. Liu, Y.L. He, S. Swaminathan, M. Rohwerder, Lin Li, Effect of dew point on the surface selective oxidation and subsurface microstructure of TRIP-aided steel, Surf. Coat. Technol. 206 (2011) 1237–1243, https://doi.org/10.1016/j.surfcoat.2011.08.038.

[17] S. Borodin, D. Vogel, S. Swaminathan, M. Rohwerder, Direct in-situ investigation of selective surface oxidation during recrystallization annealing of a binary model alloy, Oxid. Met. 85 (2016) 51–63, https://doi.org/10.1007/s11085-015-9578-8.

[18] S. Sasaki, K. Fujino, Y. Takéuchi, X-ray determination of electron-density distributions in oxides, MgO, MnO, CoO and NiO, and atomic scattering factors of their constituent atoms, P. Jpn. Acad. B-Phys. 55 (1979) 43–48, https://doi.org/10.2183/pjab.55.43.

[19] K. Fujino, S. Sasaki, Y. Takeuchi, R. Sadanaga, X-ray determination of electron distributions in forsterite, fayalite and tephroite, Acta Cryst. B37 (1981) 513–518, https://doi.org/10.1107/S0567740881003506.

[20] J.A.A. Leroux, E. Raub, Untersuchungen über das verhalten von silber und silber-Kupferlegierungen beim glühen in sauerstoff und luft, Z. Anorg. Allg. Chem. 188 (1930) 205–231, https://doi.org/10.1002/zaac.19301880119.

[21] S. Guruswamy, S.M. Park, J.P. Hirth, R.A. Rapp, Internal oxidation of Ag-in alloys: stress relief and the influence of imposed strain, Oxid. Met. 26 (1986) 77–100, https://doi.org/10.1007/BF00664274.

[22] J.R. Mackert, Metallic surface layers deposited by diffusional creep during internal oxidation, MTA 17 (1986) 746–749, https://doi.org/10.1007/BF02644001.

[23] G. Schimmel, J. Sorina-Muller, B. Kempf, M. Rettenmayr, On the mechanism of Ag exudation during internal oxidation, Acta Mater. 58 (2010) 2091–2102, https://doi.org/10.1016/j.actamat.2009.11.051.

[24] H.C. Yi, S.W. Guan, W.W. Smeltzer, A. Petric, Internal oxidation of Ni-Al and Ni-Al-Si alloys at the dissociation pressure of NiO, Acta. Met. Mat. 42 (1994) 981–990, https://doi.org/10.1016/0956-7151(94)90292-5.

[25] T. Onishi, S. Nakakubo, M. Takeda, Calculation of internal oxidation rate equations and boundary conditions between internal and external oxidation in Si containing steels, Mater. Trans. 51 (2010) 482–487, https://doi.org/10.2320/matertrans.

M2009256.

[26] M.A.A. Motin, J. Zhang, P.R. Munroe, D.J. Young, Internal oxidation and metal dusting of Fe-Si alloys, Corros. Sci. 52 (2010) 3280–3286, https://doi.org/10.1016/j.corsci.2010.05.045.

[27] D.J. Young, High Temperature Oxidation and Corrosion of Metals, 2nd edition, Elsevier, 2016.

[28] K. Nohara, K.I. Hirano, Diffusion of Mn^{54} in iron and iron-manganese alloys, proceeding ICSTIS, Suppl. Trans. ISIJ 11 (1971) 1267–1273.

[29] J. Takada, M. Adachi, Determination of diffusion coefficient of oxygen in α-iron from internal oxidation measurements in Fe-Si alloys, J. Mater. Sci. 21 (1986) 2133–2137, https://doi.org/10.1007/BF00547959.

[30] M. Oku, K. Hirokawa, X-ray photoelectron spectroscopy of Co_3O_4, Fe_3O_4, Mn_3O_4, and related compounds, J. Electron Spectrosc. Relat. Phenom. 8 (1976) 475–481, https://doi.org/10.1016/0368-2048(76)80034-5.

[31] R. Oroa, M. Camposb, E. Hryhaa, J.M. Torralbab, L. Nyborg, Surface phenomena during the early stages of sintering in steels modified with Fe-Mn-Si-C master alloys, Mater. Charact. 86 (2013) 80–91, https://doi.org/10.1016/j.matchar.2013.07.022.

[32] A. Ollivier-Leduc, M.L. Giorgi, D. Balloy, J.B. Guillot, Nucleation and growth of selective oxide particles on ferritic steel, Corros. Sci. 52 (2010) 2498–2504, https://doi.org/10.1016/j.corsci.2010.03.030.

[33] T.C. Taucher, I. Hehn, O.T. Hofmann, M. Zharnikov, E. Zojer, Understanding chemical versus electrostatic shifts in X-ray photoelectron spectra of organic self-assembled monolayers, J. Phys. Chem. C 120 (2016) 3428–3437, https://doi.org/10.1021/acs.jpcc.5b12387.

[34] A. Mekki, D. Holland, C.F. McConville, M. Salim, An XPS study of iron sodium silicate glass surfaces, J. Non-Cryst. Solids 208 (1996) 267–276, https://doi.org/10.1016/S0022-3093(96)00523-6.

[35] B.W. Veal, D.J. Lam, A.P. Paulikas, XPS study of CaO in sodium silicate glass, J. Non-Cryst. Solids 49 (1982) 309–320, https://doi.org/10.1016/0022-3093(82)90127-2.

[36] R.O. Ansell, T. Dickinson, A.F. Povey, An X-ray photo-electron spectroscopic study of the films on coloured stainless steel and coloured 'Nilomag' alloy 771, Corros. Sci. 18 (1978) 245–256, https://doi.org/10.1016/S0010-938X(78)80021-3.

[37] P. Mills, J.L. Sullivan, A study of the core level electrons in iron and its three oxides by means of X-ray photoelectron spectroscopy, J. Phys. D: Appl. Phys. 16 (1983) 723–732, https://doi.org/10.1088/0022-3727/16/5/005.

[38] N.S. McIntyre, D.G. Zetaruk, X-ray photoelectron spectroscopic studies of iron oxides, Anal. Chem. 49 (1977) 1521–1529, https://doi.org/10.1021/ac50019a016.

[39] C.E. Myers, H.F. Franzen, J.W. Anderegg, X-ray photoelectron spectra and bonding in transition-metal phosphides, Inorg. Chem. 24 (1985) 1822–1824, https://doi.org/10.1021/ic00206a025.

[40] J. Finster, E.D. Klinkenberg, J. Heeg, ESCA and SEXAFS investigations of insulating materials for ULSI microelectronics, Vacuum 41 (1990) 1586–1589, https://doi.org/10.1016/0042-207X(90)94025-L.

[41] T. Yamashita, P. Hayes, Analysis of XPS spectra of Fe^{2+} and Fe^{3+} ions in oxide materials, Appl. Surf. Sci. 254 (2008) 2441–2449, https://doi.org/10.1016/j.apsusc.2007.09.063.

[42] H. Mehrer, L. Börnstein, Numerical Data and Functional Relationships in Science and Technology: Group III, Springer, Berlin, 1990.

[43] W. Batz, H.W. Mead, C.E. Birchenall, Diffusion of silicon in iron, J. Met. 4 (1952), https://doi.org/10.1007/BF03397772 1070-1070.

[44] Thermodata, Electronic Data Bank for Thermodynamic Quantities, (2005) http://thermodata.online.fr.

[45] D. Huin, P. Flauder, J.B. Leblond, Numerical simulation of internal oxidation of steels during annealing treatments, Oxid. Met. 64 (2005) 131–167, https://doi.org/10.1007/s11085-005-5718-x.

[46] R. Abbaschian, L. Abbaschian, R.E. Reed-Hill, Physical Metallurgy Principles, fourth edition, Cengage learning, Stamford, 2008.

[47] E. Wiberg, N. Wiberg, A.F. Holleman, Inorganic Chemistry, San Diego: Academic Press; Berlin, New York: De Gruyter, 2001.